Surrogate Recycling for Structures with Spatially Uncertain Stiffness

Karl-Alexander Hoppe[a,1,*], Kevin Josef Li[a,2], Bettina Chocholaty[a,3], Johannes D. Schmid[a,4], Simon Schmid[b,5], Kian Sepahvand[a,6], Steffen Marburg[a,7]

[a]*Chair of Vibroacoustics of Vehicles and Machines, School of Engineering and Design, Technical University of Munich, Boltzmannstraße 15, Garching bei München, 85748, Bavaria, Germany*
[b]*Chair of Non-Destructive Testing, School of Engineering and Design, Technical University of Munich, Franz-Langinger-Straße 10, München, 81245, Bavaria, Germany*

Abstract

This study expands the existing methods for non-destructively identifying the spatially varying material properties of a structure using modal data. It continues a recently published approach to this inverse problem that employed Bayesian inference in conjunction with the Karhunen-Loève expansion to solve it. Here, we present two developments. Firstly, eigenvectors are used instead of eigenvalues, improving the results significantly. Secondly, a generalized polynomial chaos surrogate accelerates the inversion procedure. Finally, we develop a methodology for reusing the surrogate model across inversion tasks. We demonstrate the efficacy and efficiency of this methodology via the field of additive manufacturing and the fused deposition modeling process. The good results promise profound computational cost saving potential for large-scale applications.

Keywords: material parameter identification, modal analysis, finite element method, generalized polynomial chaos, Bayesian inference, Karhunen-Loève expansion, process-structure-property relations, functionally graded material

---

1. Introduction

Non-homogeneous materials are receiving increasing attention from researchers. Owing to advances in computational power, naturally non-homogeneous materials and those, where the

---

*Corresponding author
Email address:* `alexander.hoppe@tum.de` (Karl-Alexander Hoppe)
[1]`https://orcid.org/0000-0002-3048-8284`
[2]`https://orcid.org/0000-0002-5885-0863`
[3]`https://orcid.org/0000-0003-3840-5946`
[4]`https://orcid.org/0000-0002-7106-2407`
[5]`https://orcid.org/0000-0002-7509-6217`
[6]`https://orcid.org/0000-0001-6952-250X`
[7]`https://orcid.org/0000-0001-6464-8015`

manufacturing process induces unintentional non-homogeneity, see Gupta and Gupta [1], are being regarded. On the other hand, functionally graded materials are being popularized, see Garcia et al. [2], which creates demand for corresponding testing methods. With functionally graded materials, the material parameters are varied spatially with intent. Marzouk and Najm [3] develop a method that is useful for characterizing such a material and Uribe et al. [4] apply a related method successfully to the identification of spatially varying stiffness using static deflection data of a structure.

Sundararajan et al. [5] report that the material non-homogeneity significantly influences the vibration behavior of functionally graded plates. As a response to this, Hoppe et al. [6] propose a non-destructive resonance frequency method for identifying the spatially varying stiffness of structures. Frequency response functions at several observation points improve the estimation of the piece-wise non-homogeneous Young's modulus. [7, 8] Batou and Soize [9] extend this procedure to account for continuously non-homogeneous materials in composite structures.

The framework by Marzouk and Najm [3] demands that the covariance of the spatially varying material property is known. Sraj et al. [10] propose a procedure that eliminates the requirement of having *a priori* knowledge of the covariance hyper-parameters using this established Bayesian inference framework in conjunction with the Karhunen-Loève expansion and generalized polynomial chaos expansion. Siripatana et al. [11] accelerate this procedure by adding a second, nested generalized polynomial chaos surrogate. However, these studies assume that the covariance hyper-parameters of the unknown spatially varying quantity are notoriously intangible.

Indeed, the linkage between manufacturing process parameters and the properties of the manufactured parts continues to elude researchers. The following paragraphs ponder why process-structure-property relations, that is the impact of process parameters on part properties, are so hard to identify within the scope of additive manufacturing.

Complexity must be mentioned as the first inhibitor. Hashemi et al. [12] stress that the knowledge of the underlying physics is incomplete. Non-linearity is notoriously hard to capture in the context of additive manufacturing, and excitation as well as boundary conditions are not approximated well enough, see Gatsos et al. [13]. Not only are the process-structure-property relations complex, so are the process parameters themselves [14, 15, 16]. On top of that, often more than 10 process parameters exhibit a relevant impact [12]. Models need to be harmonized across scales

2

and time-scales [17]. In addition to being cost and time-intensive, the necessary experiment chains and cohesive multi-scale approaches [18, 19] are prone to error propagation.

Secondly, the completeness and lack thereof present a recurring theme in the literature. A perpetual dichotomy seems to be present in the literature. It is often stated that a substantial amount of work has been completed, but that significant gaps remain [18, 20]. Specifically, many physical phenomena have yet to be examined, more materials and manufacturing processes should be studied, and a broader range of process-structure-property relations are to be investigated, see Patham and Foss [21]. In general, more experimental and high-fidelity numerical data that are transparent and accessible are needed [21].

Finally, process-structure-property relations are plagued by uncertainties. The lack of deterministic process-structure-property relations stems from the aleatory uncertainty that part properties entail and the epistemic uncertainty connected to physics-based models [22, 23]. There exists considerable interest in the statistical information entailed by materials and their processing, where the correlations of the process-structure-property relations have yet to be established [24].

The integrated computational materials engineering framework proposed by Horstemeyer and Sahay [25] is a design approach that attempts to connect material models across different scales. Ghosh [26] predicts that multi-scale modeling will accelerate the discovery of the correlations of process-structure-property relations within the integrated computational materials engineering framework. They anticipate this to be achieved by the generation of large amounts of data and the subsequent completion of process-structure-property relations via data-driven methods.

We suggest an abstraction that may serve as a remedy. While process-structure-property relations continue developing, we instead consider the random field length-scales of the manufacturing process and the manufactured part, respectively. A link between these two random field length-scales is significantly easier to establish than a direct one between the corresponding parameters. Especially when the material parameter is a linear, albeit unknown function of the process parameter, the length-scale of the latter as a Gaussian process propagates to the material parameter. We leverage this link to accelerate the inference of spatially varying material parameters of parts designed to meet different requirements that are configured similarly. For the additive manufacturing process fused deposition modeling [27, 28, 29], which uses plastics as a material, we train a surrogate for one set of hyper-parameters and then recycle this surrogate for modified configurations of

the part.

This paper is organized as follows: Section 2 presents the theoretical preliminaries for our non-destructive material parameter identification workflow. These concepts are applied to the identification of spatially varying stiffness given a structure's modal data in Section 3. This section demonstrates the novel methodology, where the surrogate used for stiffness identification is trained using one configuration and recycled for the others. The results of this demonstrator are presented in Section 4 and discussed in Section 5, where we also draw conclusions from our findings.

2. Methods for Inferring Dimensionality-Reduced Random Fields Employing Surrogate Models

This section covers all relevant methods necessary for the generation of our results in Section 4. Section 2.1 formulates the Bayesian inverse problem setup, Section 2.2 describes the reduction of the random space via the Karhunen-Loève expansion, and Section 2.3 briefly covers how the generalized polynomial chaos surrogate is constructed on this dimensionality-reduced space. Finally, Section 2.4 details the transformation of the generalized polynomial chaos surrogate when the Karhunen-Loève expansion, whose coefficients are the surrogate inputs, changes.

2.1. Inverse Problem Setup Using the Bayesian Approach

Consider an ideal forward model $\mathbf{G}$

$$\mathbf{d} = \mathbf{G}(\mathbf{m}) + \boldsymbol{\epsilon}, \tag{1}$$

where $\mathbf{d}$ is the data, $\mathbf{m}$ are the model parameters, and $\boldsymbol{\epsilon}$ is independent and ideally distributed Gaussian measurement noise. Given the data $\mathbf{d}$ and the forward model, solving the inverse problem is to estimate the unknown model parameters. One way of solving an inverse problem is the Bayesian approach. Bayes' rule reflects how new data updates our prior beliefs, formulated as the prior probability distribution $\rho(\mathbf{m})$, concerning the unknowns $\mathbf{m}$. Expressing these quantities in terms of probability densities produces Bayes' theorem

$$\pi_m(\mathbf{m}) = \rho(\mathbf{m}|\mathbf{d}) \propto \rho(\mathbf{d}|\mathbf{m})\rho(\mathbf{m}), \tag{2}$$

stating that the posterior probability density $\rho(\mathbf{m}|\mathbf{d})$ of the model parameters given the data is proportional to the product of likelihood and prior probability density. The likelihood

$$\mathcal{L}(\mathbf{m}) = \rho(\mathbf{d}|\mathbf{m}) = \rho_\epsilon(\mathbf{d} - \mathbf{G}(\mathbf{m})) \tag{3}$$

4

measures how likely an observation of the data $\mathbf{d}$ is, given the model parameters $\mathbf{m}$.

Sampling from the posterior distribution is often achieved with exploration algorithms. The samples approximate the true posterior density and allow for the calculation of statistical moments. A computationally cheaper strategy is finding the mode of the posterior probability density by solving an optimization problem. This approach, which explicitly does not estimate the expected value, is called the maximum a posteriori estimate:

$$\mathbf{m}_{\text{MAP}} = \arg \max \, \mathcal{L}(\mathbf{m})\rho(\mathbf{m}). \tag{4}$$

2.2. Karhunen-Loève Expansion

When identifying the properties of homogeneous materials, the parameters are typically interpreted as random variables in the context of Bayesian inference. For non-homogeneous materials, the material parameters are spatially varying and are considered as functions that live on the spatial domain of the structure. Fine discretization of these functions yields a large number of unknowns that have to be identified in the inversion procedure. This collection of random variables can be described as a random field. Second order random fields are fully described by their mean and covariance functions. The covariance function of two points $\mathbf{x}$ and $\mathbf{x}'$ reads as

$$C(\mathbf{x}, \mathbf{x}') = \sum_{i=1}^{K} \lambda_i \phi_i(\mathbf{x})\phi_i(\mathbf{x}') \quad \text{with} \quad \|\phi_i\| = 1 \tag{5}$$

and is decomposable using its eigenvalues λ_i, eigenfunctions ϕ_i, and K terms.

Having to approximate a high-dimensional multi-variate distribution is detrimental to the inversion procedure, as the inference must then traverse this high-dimensional space. Mercer's theorem 5[30], which the Karhunen-Loève expansion is based on, offers a remedy. The Karhunen-Loève expansion of a random field coincides with a dimensionality reduction of the random space. Specifically, the random dimensionality is decoupled from the spatial discretization and reduced to the truncation order K. The truncated Karhunen-Loève expansion reads as

$$M_K(\mathbf{x}, \omega) = \boldsymbol{\mu}(\mathbf{x}) + \sum_{i=1}^{K} \sqrt{\lambda_i}\eta_i(\omega)\phi_i(\mathbf{x}). \tag{6}$$

Here, M is a Gaussian second order random field, $\boldsymbol{\mu}$ is the mean function, and η_i are the Karhunen-Loève coefficients. Now, η_i represent the new finite collection of random variables that encapsulate the random field's variability by means of the Karhunen-Loève expansion. They can be used to generate realizations of the random field when sampled from standard normal distributions.

2.3. Dimensionality-Reduced Generalized Polynomial Chaos

Marzouk and Najm [3] pioneer the combination of the Karhunen-Loève expansion with generalized polynomial chaos in the context of Bayesian inference. The use of generalized polynomial chaos as a surrogate is beneficial when forward model evaluations are computationally expensive. This is especially relevant for methods employing Markov chains for the posterior's exploration.

The goal of the generalized polynomial chaos expansion within this scope is to construct a computationally less expensive surrogate for the forward model $\mathbf{G}(\boldsymbol{\eta})$. This surrogate employs both, an expansion of the forward model inputs

$$\hat{\eta}_i = g_i(\boldsymbol{\xi}) = \sum_{k=0}^{N_{P1}} a_{ik} \Psi_k(\boldsymbol{\xi}) \tag{7}$$

and an expansion of the forward model outputs

$$\hat{G}_i = \sum_{k=0}^{N_{P2}} b_{ik} \Psi_k(\boldsymbol{\xi}). \tag{8}$$

Here, the number of terms

$$N_p + 1 = \frac{(n+p)!}{n!p!} \tag{9}$$

depends on the polynomial order p and the number n of input random variables $\boldsymbol{\xi}$. When the Karhunen-Loève coefficients comprise the model inputs, an optimal generalized polynomial chaos expansion can be achieved by using Hermite polynomials for the polynomial basis Ψ, as the Karhunen-Loève coefficients are standard normally distributed. After obtaining the generalized polynomial chaos coefficients $\mathbf{a}$ and $\mathbf{b}$ using stochastic collocation, drawing samples from $\boldsymbol{\xi}$ and evaluating the generalized polynomial chaos surrogate $\hat{\mathbf{G}}(\boldsymbol{\xi})$ accordingly yields response samples that approximate the true model response.

2.4. Removing the Surrogate Model's Dependence on the Random Field Hyper-Parameters

A new generalized polynomial chaos surrogate must be computed, when the parametrization of the Gaussian process prior on the quantity of interest changes. When the covariance hyper-parameters of the random field change, so does its Karhunen-Loève expansion, as the eigenvalues and eigenvectors are updated. Because the generalized polynomial chaos surrogate utilizes an expansion of the Karhunen-Loève coefficients to construct the generalized polynomial chaos expansion of the model outputs, it must be trained anew. Sraj et al. [10] resolve this dependency and develop

a more flexible variant of the Karhunen-Loève expansion that need not be recomputed when the covariance hyper-parameters change. In the following paragraphs, we briefly summarize the study by Sraj et al. [10], as it is not uniformly known within the community.

The transformation from one parametrization of a covariance function to another by leveraging the projection of their respective eigenfunctions onto each other lies at the core of their method. It is the aim to transform from a reference covariance $C(\mathbf{q}^r) = C^r$ with a set of reference hyper-parameters $\mathbf{q}^r$ to a covariance endowed with different hyper-parameters. After being projected onto them, the new eigenfunctions $\Phi_i(\mathbf{q})$ can be expressed in terms of the reference eigenfunctions

$$\Phi_i(\mathbf{q}) = \sum_{i'=1}^{\infty} b_{ii'}(\mathbf{q})\phi_{i'}^r \quad \text{with} \quad b_{ii'} = (\phi_i^r, \Phi_{i'}(\mathbf{q}))_X . \tag{10}$$

These so-called scaled eigenfunctions are defined in the context of the target covariance as the product of its eigenvalues and eigenfunctions

$$\Phi(\mathbf{q})_i = \sqrt{\lambda_i(\mathbf{q})}\phi_i(\mathbf{q}). \tag{11}$$

The Karhunen-Loève expansion corresponding to the target covariance can now be expressed in terms of the reference covariance as

$$M_K(\omega, \mathbf{q}) = \sum_{i=1}^{K} \Phi_i(\mathbf{q})\eta_i(\omega) \approx \sum_{i=1}^{K} \left(\sum_{i'=1}^{K} b_{ii'}(\mathbf{q})\phi_{i'}^r \right) \eta_i(\omega) = \sum_{i=1}^{K} \phi_i^r \eta_i^{\text{ct}}(\omega, \mathbf{q}). \tag{12}$$

The transformed Karhunen-Loève coefficients

$$\eta_i^{\text{ct}}(\omega, \mathbf{q}) = \sum_{i'=1}^{K} b_{i'i}(\mathbf{q})\eta_{i'}(\omega) \tag{13}$$

are found using the reference Karhunen-Loève coefficients and the projection coefficients $b_{ii'}$. They read as

$$\boldsymbol{\eta}^{\text{ct}}(\omega, \mathbf{q}) = \mathcal{B}(\mathbf{q})\boldsymbol{\eta}(\omega) \tag{14}$$

in matrix form. Finally, a transformed surrogate is obtained, where the transformed generalized polynomial chaos expansion of the inputs reads as

$$G_j(\boldsymbol{\eta}, \boldsymbol{q}) = G_j^r \approx \hat{G}_j^r (\boldsymbol{\xi}(\boldsymbol{\eta}, \mathbf{q})) = \sum_{i=0}^{N_p} a_{ji}\psi_i(\boldsymbol{\xi}(\boldsymbol{\eta}, \mathbf{q})) \quad \text{with} \quad \boldsymbol{\xi}(\boldsymbol{\eta}, \mathbf{q}) = \hat{\mathcal{B}}(\mathbf{q})\boldsymbol{\eta}, \tag{15}$$

where the $\hat{\mathcal{B}}$-matrix is defined as

$$\hat{\mathcal{B}}(\mathbf{q}) = \begin{cases} \frac{\mathcal{B}_{kl}(\mathbf{q})}{\sqrt{\lambda_k^r}} & \text{if } \frac{\lambda_k^r}{\lambda_1^r} > \kappa \text{ with } \kappa \approx 1 \times 10^{-12}, \\ 0 & \text{otherwise.} \end{cases} \tag{16}$$

This transformed surrogate is trained on the reference covariance, as it reuses the corresponding generalized polynomial chaos coefficients and applies a transformation to the input random variables $\boldsymbol{\eta}$. It may be used to approximate a system whose input random field is described by a different covariance function, termed the target covariance.

The relative error ε_M between a random field M and its transformed representation M_K^{ct} reads as

$$\varepsilon_M(K, \mathbf{q}) = \frac{\|M(\mathbf{q}) - M_K^{\text{ct}}(\mathbf{q})\|_{L^2(\Omega, D)}}{\|M(\mathbf{q})\|_{L^2(\Omega, D)}}, \tag{17}$$

where

$$\|U\|_{L^2(\Omega, D)}^2 \doteq \mathbb{E}\left[(U, U)_X\right]. \tag{18}$$

The left graph within Figure 1 shows this error for $K = 15$, a squared exponential kernel with variance $\sigma^2 = 0.5$, and varying parametrization $\mathbf{q} = l$. The right graph shows the square root of $\beta_{\max}(\mathbf{q})$, the largest eigenvalue of the covariance matrix $\hat{\Sigma}^2(\mathbf{q}) = \hat{\mathcal{B}}^T(\mathbf{q})\hat{\mathcal{B}}(\mathbf{q})$.
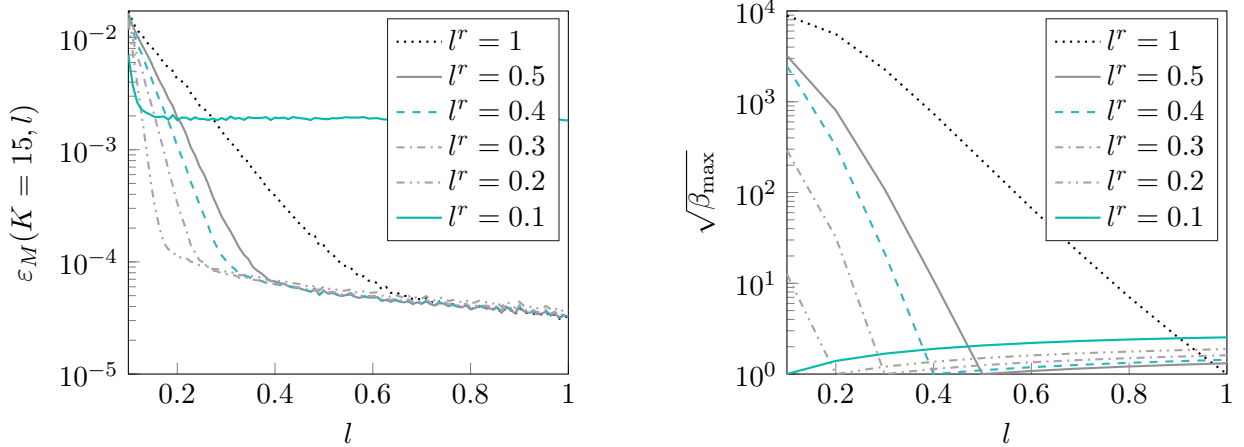

Figure 1: Relative error ε_M and $\sqrt{\beta_{\max}}$ for a range of ratios between reference and transformed random field, following Sraj et al. [10].

3. Procedure

3.1. Preliminary Study and Proof of Concept: Dimensionality-Reduced and Generalized Polynomial Chaos-Accelerated Inference of Young's Modulus Using Mode Shape Data

In this section, we apply the accelerated and dimensionality-reduced inference procedure by Marzouk and Najm [3] to the non-destructive identification of spatially varying stiffness given mode shape information.

We present our application as a preliminary study and proof of concept for our methodology that will be introduced later. The quantity of interest is a random function defined on one spatial dimension. It represents the Young's modulus in x-direction $E_x(x)$ of a beam measuring $x \times y \times z = 450 \times 60 \times 9\,\mathrm{mm}$ with free-free boundary conditions. The numerical modal analysis is carried out in a python-based finite element method software [31] with a structured mesh and 5472 quadratic elements. The first eigenvector of the structure obtained from performing numerical modal analysis given the ground truth Young's modulus makes up the synthesized measurement data. A signal-to-noise ratio of $60\,\mathrm{dB}$ describes the simulated independent and identically distributed Gaussian measurement noise. The reader is referred to Figure 2 for a visual representation of our procedure and especially the scope of the surrogate model.
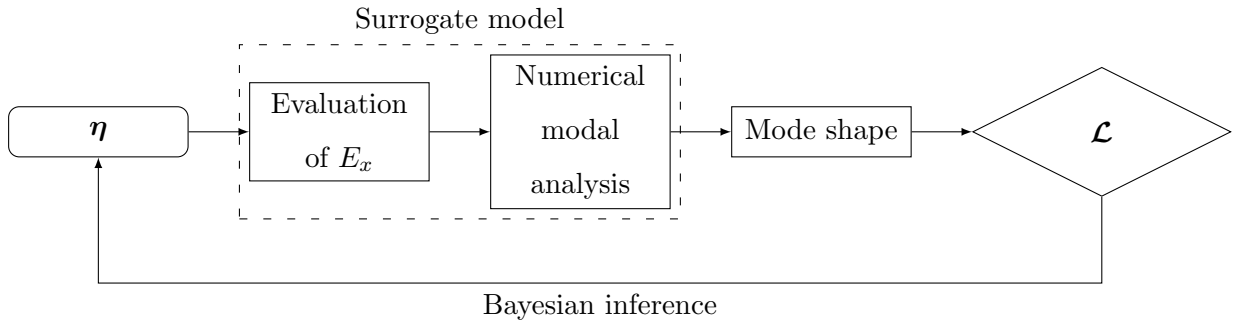

Figure 2: General procedure for reconstructing the reference random field given a mode shape and assuming the covariance, priors, and measurement noise characteristics with Bayesian inference. The Karhunen-Loève coefficients $\boldsymbol{\eta}$ are the quantities of interest. Within each step of the Bayesian inference sequence, the evaluation of the Karhunen-Loève expansion with these coefficients yields E_x with the full spatial resolution. Numerical modal analysis is carried out using this E_x assigned within the finite element model, yielding the beam's first mode shape. The inference uses a generalized polynomial chaos surrogate here that connects $\boldsymbol{\eta}$ to a probe grid for the first mode shape. Upon comparison with the noisy measurement using the likelihood $\mathcal{L}$, this step within the Bayesian inference is complete and a new sample of $\boldsymbol{\eta}$ is drawn subsequently.

9

The material's statistical moments read as follows: The Young's modulus $E_x(x)$ is described by a mean $\bar{E}_x$ of $3\,\mathrm{MPa}$ and a standard deviation of $\sigma_{E_x} = 1\% \times \bar{E}_x$. The material is modeled as a random field over x and endowed with a Gaussian process prior with a Matérn covariance kernel [32]

$$C(\mathbf{x}, \mathbf{x}') = \sigma^2 \frac{2^{1-\nu}}{\Gamma(\nu)} \left(\frac{\sqrt{2\nu}|\mathbf{x} - \mathbf{x}'|}{l} \right)^{\nu} K_\nu \left(\frac{\sqrt{2\nu}|\mathbf{x} - \mathbf{x}'|}{l} \right), \tag{19}$$

where $\Gamma(\nu)$ denotes the gamma function and K_ν is a modified Bessel function [33]. The smoothing parameter and correlation length are set to $\nu = 3/2$ and $l = L_2 = 450\,\mathrm{mm}$, respectively. The second order generalized polynomial chaos expansion is used in conjunction with a Karhunen-Loève expansion truncated to 5 terms. The Karhunen-Loève coefficients $\boldsymbol{\eta}$ are appropriately equipped with standard normal prior distributions, since $\boldsymbol{\eta} \sim \mathcal{N}(0, 1)$. We use a non-normalized logarithmic likelihood

$$l(X_{\mathrm{meas}}|\boldsymbol{\eta}) = -\frac{1}{2} \sum_{j=1}^{N} \frac{\left(X_{\mathrm{meas}_j} - \hat{\mathbf{G}}_j(\boldsymbol{\eta}) \right)^2}{\epsilon_j^2}, \tag{20}$$

where $N = 522$ is the number of evaluation points at the top of the geometry within the finite element model. Here, the likelihood variances are set equal to the measurement noise ϵ, which is obtained by applying the signal-to-noise ratio to the deterministic ground truth simulation mode shape data. The synthetic measurement is carried out 10 times in total.

3.2. Application of the Methodology to Material Parameter Identification for Functionally Graded Fused Deposition Modeling Parts

This section introduces the manufacturing process and the material models used in the academic example. It describes the chosen part configurations used in the example, see Section 3.2.1, and the process parameters together with the estimation of their length scales, see Section 3.2.2. Finally, Section 3.2.3 introduces uncertainty into the material parameters.

In the following, we demonstrate how, given a correlation between process and part parameter length-scales, the knowledge of the former enables surrogate model recycling. This procedure exhibits significant computation cost improvements over existing procedures as soon as a part is designed for more than one configuration. It relies on the combination of the Karhunen-Loève expansion and generalized polynomial chaos within Bayesian inference. The novel interpretation of the coordinate transformation described in Section 2.4 makes it possible to reuse a surrogate for configurations other than the reference configuration.
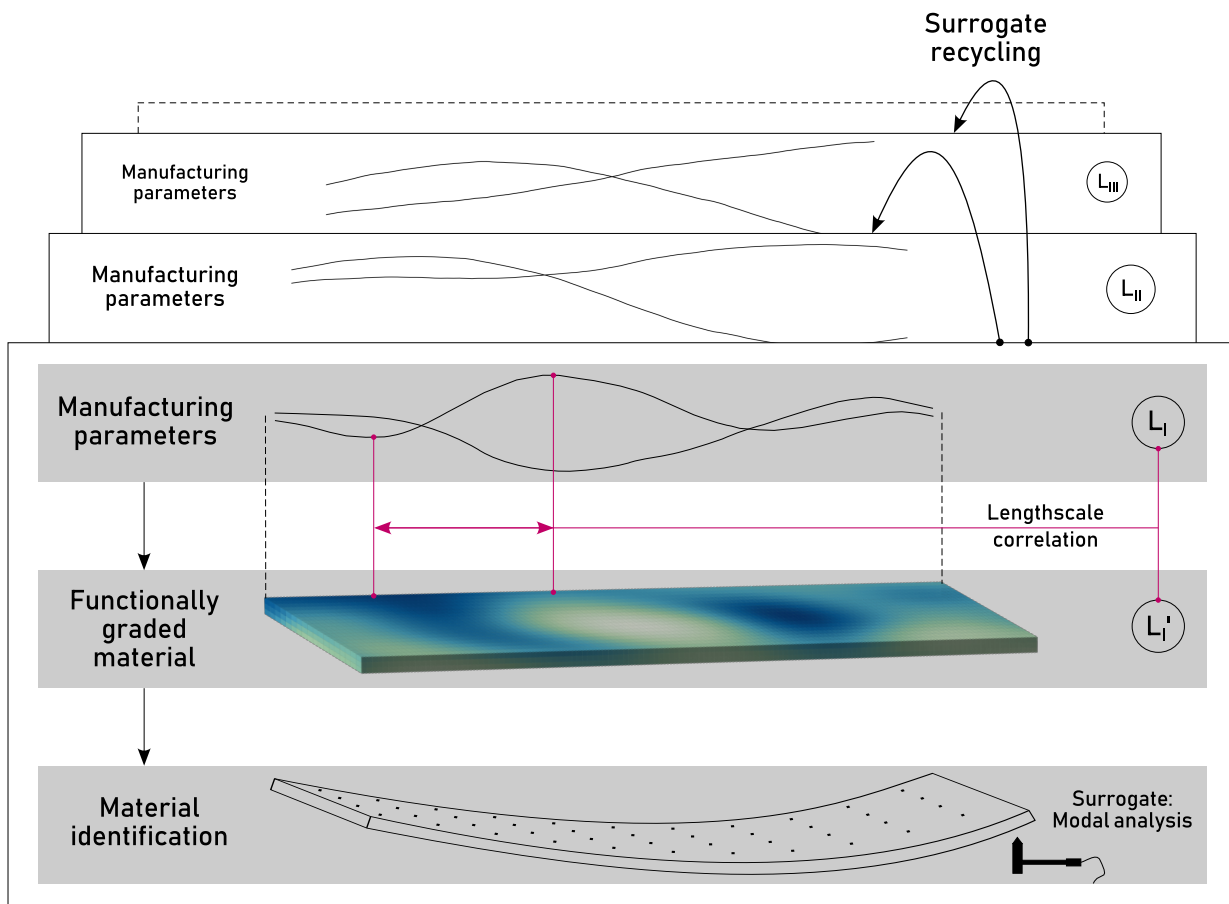
Figure 3: The figure shows the proposed novel methodology for recycling surrogate models connecting spatially random materials to a structure's mode shape. The recycling is employed based on length-scale correlations between the manufacturing process parameters on the one hand and the resulting material properties on the other hand. This procedure is embedded into the non-destructive material parameter identification that uses a Bayesian approach for solving the inverse problem.

3.2.1. Part Configurations

The goal for the considered manufacturing process is to produce three geometrically identical parts that are designed for distinct applications. In the context of large assemblies, interfaces dominate the development cost. If the production volume is high, the production cost is equally affected. The flexibility of application while maintaining the cost-sensitive compliance with interface requirements is enabled through the functional grading realized with the fused deposition modeling process and filaments A and B. The optimized, functionally graded parts offer surplus yield strength in regions with high equivalent stresses and reduce the yield stress in locations where high strength is not a requirement. The theoretically resulting deterministic stiffness profiles improve the minimum safety of the assembly for the functionally graded parts in comparison to the homogeneous parts. On the one hand, this may be used to reduce weight while retaining the safety, on the other hand, the safety-margin can be improved at constant part mass. The latter is pursued here, as keeping the overall part mass constant reduces the need for load bearing changes in the overall assembly due to changes in the part mass, thus further lowering costs.

All configurations involve a structural beam with dimensions $450 \times 60 \times 9\,\text{mm}$. Each of the three functionally graded beams is designed to meet the changing requirements posed by a different application configuration. For the demonstration, we vary the external loads and the boundary conditions.

- Configuration 1, shown in Figure 4, is a cantilever beam with a clamping on the left side and the load located on the right side at the free end. An equivalent one-dimensional and homogeneous system exhibits a linear bending moment curve M_B, as marked in the figure with contrasting styling. Designing a material with properties appropriate for the stress decreasing together with the distance from the clamping requires a matching grading of the yield stress. Choosing a linear yield stress curve leads to the largest length-scale considered in this study.

- Configuration 2, shown in Figure 4, is a cantilever beam with a clamping on the left side and a free tip, which is subject to a line load p. An equivalent homogeneous one-dimensional system exhibits a bending moment curve M_B proportional to the trunk of a parabola, as the contrasting line displays. Designing a material with an according grading of the yield stress necessitates a decreasing yield stress with growing distance from the clamping. The volume

12

fractions are endowed with a medium correlation length to assimilate half of a parabolic curve in the material parameters.

- Configuration 3, shown in Figure 4, involves a beam with the pinned boundary condition on the left side and a roller bearing at the right end. Subjected to a line load, an equivalent one-dimensional and homogeneous system possesses a parabolic bending moment curve M_B that is plotted with a contrasting color. Designing a material with an according grading of the yield stress requires the maximum yield stress to be at the center between the bearings and the minimum yield stresses to be located at the bearings. Here, the smallest length-scale investigated in this study is appropriate for the described yield stress distribution.
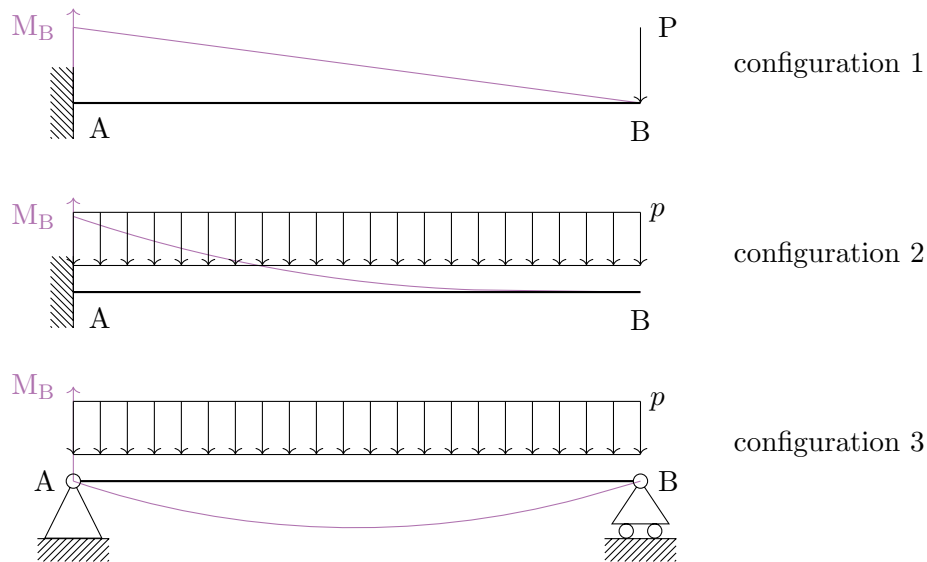

Figure 4: Part design configurations: For configuration 1, the cantilever beam is clamped on the left side and subject to a load located at the free end on the right. In configuration 2, the cantilever beam is clamped on the left side and subject to a line load acting on the entire domain. In configuration 3, the beam is pinned on the left side and has a roller bearing on the right side. Again, a line load acts on the entire domain.

As a reference for the virtual functionally graded parts, consider a virtual traditional homogeneous part made of a typical additive manufacturing thermoplastic, see Table 1, whose Young's modulus is expected as 3×10^3 MPa. For the functionally graded parts, consider two materials, of which filament A is less stiff than the baseline material with 2.5×10^3 MPa, while filament B is stiffer than the baseline with 3.5×10^3 MPa. The average stiffness and mass density of filaments A and B are equal to that of the baseline material for the sake of comparability. This in

turn necessitates also fictitious filaments, as no existing materials fulfill this equality constraint

195 perfectly.

	Homogeneous material
Name	ABS
Young's modulus	$3 \times 10^3 \,\mathrm{MPa}$
Yield stress	$48.3 \,\mathrm{MPa}$
Density	$1190 \,\mathrm{kg\,m^{-3}}$

Table 1: This table lists the characteristics of the exemplary homogeneous material that serves as the material for the baseline parts and thus as a reference for the functionally graded parts. Specifically, the popular additive manufacturing thermoplastic ABS is chosen to be the reference in terms of density and stiffness.

	Filament A	Filament B
Young's modulus	$2.5 \times 10^3 \,\mathrm{MPa}$	$3.5 \times 10^3 \,\mathrm{MPa}$
Yield stress	$40.3 \,\mathrm{MPa}$	$56.4 \,\mathrm{MPa}$
Density	$992 \,\mathrm{kg\,m^{-3}}$	$1390 \,\mathrm{kg\,m^{-3}}$

Table 2: This table presents the Young's modulus, yield stress, and density of the two exemplary materials used in the fused deposition modeling process. Filament A has 5/6 of the homogeneous material's stiffness and density, while filament B has 7/6 of the homogeneous material's stiffness and density. Filament A is thus the less stiff and dense component and filament B provides higher stiffness at the drawback of increased density.

3.2.2. Fused Deposition Modeling

Our academic example is centered around fused deposition modeling, see Figure 5. Fused deposition modeling is a multi-material additive manufacturing process categorized within material extrusion. Thermoplastic polymers make up the most common stock material for this process.

200 Typically dual nozzle systems are employed, where a separate feed mechanism passes through the extrusion head for each of the two filaments. The building strategy consists of assigning a filament type to each position on the build bed. Consequently, the smoothness of the functional grading at the macro-scale depends on the spatial resolution of the building strategy [29].

For simplicity, we consider the positional volume fractions resulting from the building strategy

205 as the process parameters in this study and assume that their length-scales match those of the
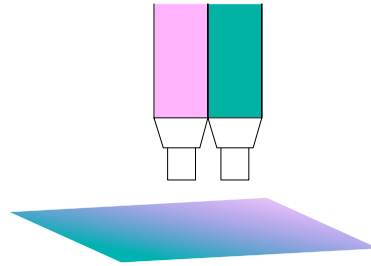
14

compound material parameters.

Figure 5: Sketch of the fused deposition modeling principle. The jet shown at the top of the image is capable of producing a part, which is shown at the bottom, whose material distribution is functionally graded.

The building strategy involving filaments A and B tailors the part to the specific application configuration via functional grading. Figures 6 and 7 show possible volume fraction designs for both materials that need to be accomplished by the building strategy for all configurations. Here, the material strength is shifted towards regions with high stresses, while the overall mass stays constant.
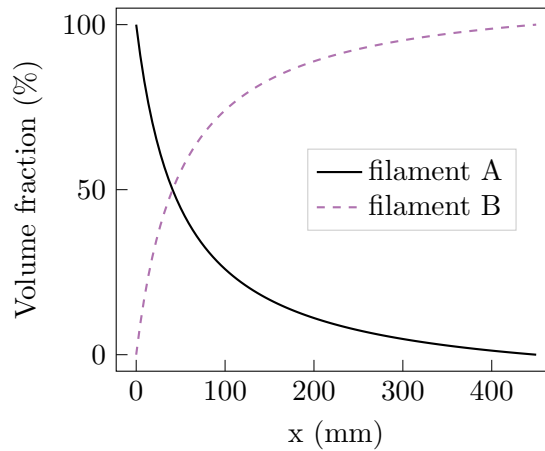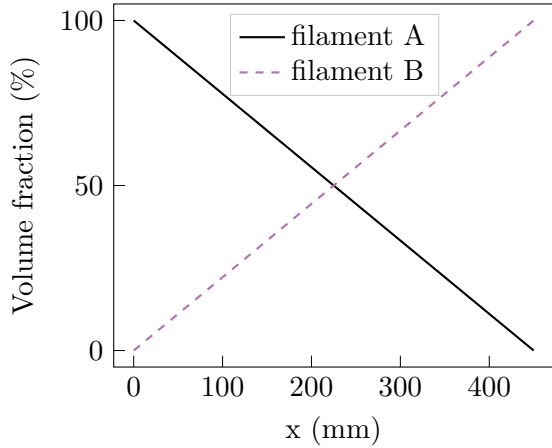

Figure 6: Configuration 2 (reference): Here, the volume fraction corresponding to filament A decreases hyperbolically, while that of filament B constitutes the remainder. These volume fractions represent the ideal deterministic volume fractions that correspond to the ideal deterministic stiffness profiles and that are not manufacturable in practice.

In practice, the length-scale of the volume fractions is readily estimated with Gaussian process regression while considering this length-scale to be uncertain. A naïve estimate thereof suffices for this demonstration. The variability of the profile for configuration 1 is the smallest, while it increases for configuration 2 and increases further for configuration 3. With this observation, we

(a) Configuration 1: Here, the volume fraction corresponding to filament A decreases linearly, while that of filament B increases linearly.
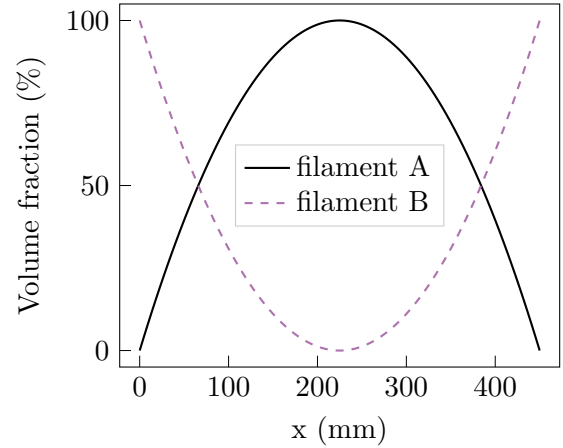
(b) Configuration 3: Here, the volume fraction corresponding to filament A follows a parabola opening downward, while that of filament B follows a parabola opening upward.

Figure 7: The figures show the material volume fractions over the beams' x-coordinate for the altered configurations. These volume fractions represent the ideal deterministic volume fractions that correspond to the ideal deterministic stiffness profiles and that are not manufacturable in practice.

arrive at the estimated length-scales reported in Table 3.

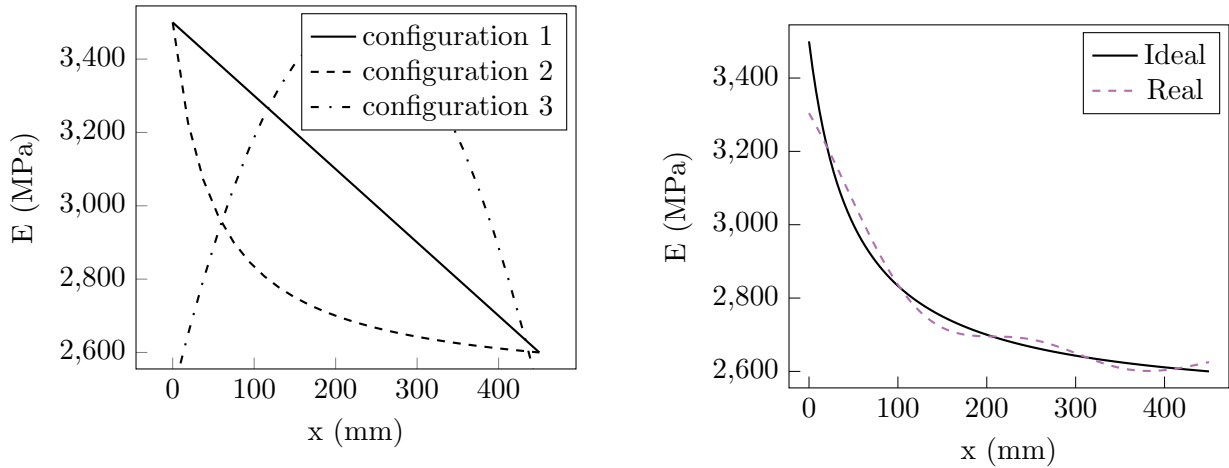|	configuration 1	configuration 2	configuration 3
Length-scale	$L_1 = 900\,\mathrm{mm}$	$L_2 = 450\,\mathrm{mm}$	$L_3 = 225\,\mathrm{mm}$

Table 3: The table lists the naïve length-scale estimates for each configuration. The volume fractions' length-scales pose the optimal choice for the priors on the material parameter length-scales and care should be taken to correctly identify them. For our academic problem, we assume these length-scales to be known by projecting the stiffness profiles onto the eigenfunctions of a covariance function with the respective length-scale.

3.2.3. Assumption of the Manufacturable Stiffness Profiles as Realizations of Gaussian Processes

In theory, with a deterministic linear manufacturing process and deterministic materials, the shown material volume fractions translate into Young's modulus functions over x assuming a linear volumetric Young's modulus law. Figure 8a shows the corresponding stiffness profiles for configuration 1, configuration 2, and configuration 3. These present the ideal aggregated stiffness profiles that raise the minimum safety-margin and retain the mass.

In practice, the properties of the manufactured parts are not deterministic. Instead, they are subject to uncertainty. We model the manufacturable stiffness profiles as realizations of Gaus-

16

sian processes. To achieve this, the ideal stiffness profiles are individually approximated with a Karhunen-Loève expansion with truncation order of $K = 5$, with the covariance from Eq. (19), and the matching length-scales from Table 3. Figure 8b shows the manufacturable stiffness profile for the reference configuration, while Figure 9 shows the corresponding profiles for configuration 1 and configuration 3. The realizable stiffness for configuration 1 shows a close agreement throughout the beam with the original stiffness, while the realizable stiffness for configuration 2 fails to capture the desired stiffness peak at the clamping. The chosen random space discretization overestimates the minimum stiffness values at the beam's boundaries for configuration 3. Overall, the characteristics of the ideal profiles are captured well. The approximation of the configuration 1 profile being the most accurate demonstrates that retaining more terms in the Karhunen-Loève expansion would enable the projection to capture even more of the ideal profiles' variance.


(a) Deterministic target design Young's modulus profiles for configuration 1, configuration 2, and configuration 3, respectively. The solid line corresponds to configuration 1, the dashed line corresponds to configuration 2, and the dashed-dotted line corresponds to configuration 3.

(b) Configuration 2 (reference): The target stiffness projected onto the first 5 eigenfunctions of a covariance with L_2 is indicated by the dashed line, while the solid line shows the ideal stiffness.

Figure 8: Deterministic target design Young's modulus profiles for all configurations and manufacturable stiffness for the reference configuration.
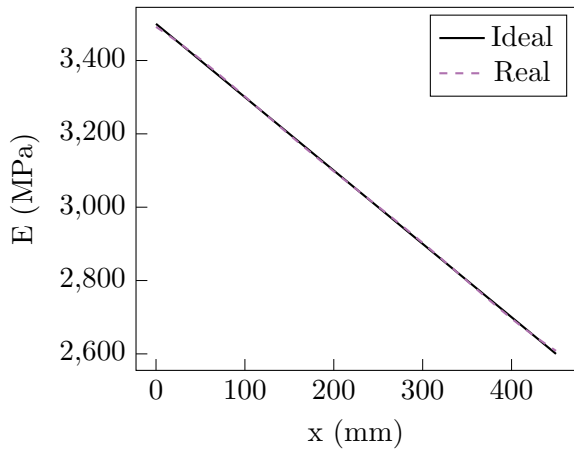
(a) Configuration 1: The deterministic target stiffness projected onto the first 5 eigenfunctions of a covariance with L_1 is indicated by the dashed line and the ideal stiffness is marked with a solid line.
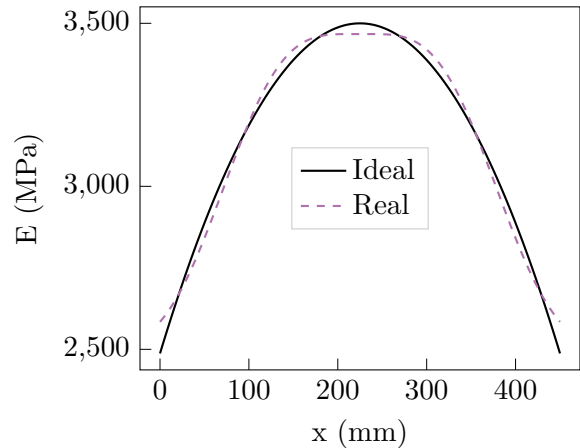
(b) Configuration 3: Manufacturable stiffness profile subject to uncertainty as the realization of a Gaussian process. The dashed line marks the projection of the deterministic stiffness onto the first 5 eigenfunctions of a covariance function with length-scale L_3. The solid line indicates the ideal stiffness.

Figure 9: Manufacturable stiffness profiles subject to uncertainty as Gaussian process realizations for configuration 1 and configuration 3.

4. Results

4.1. Dimensionality-Reduced and Generalized Polynomial Chaos-Accelerated Inference of Young's Modulus Using Mode Shape Data

The surrogate shortens the inversion procedure duration from more than 170 to less than 1.7 seconds on consumer-grade hardware. Now, the bulk amount of CPU time is spent evaluating the likelihood instead of the model, as is the case when using the full finite element model. The inference results for the Young's modulus E_x using maximum a posteriori estimation agree excellently with the ground truth, see Figure 10. This clearly demonstrates the efficiency and efficacy of our proposed method for identifying the spatially varying Young's modulus of a structure using mode shape data.

4.2. Surrogate Recycling Results

This section first presents the effect of using the functionally graded material as opposed to homogeneous material on the safety-margin within static loading. Following this, the spatially
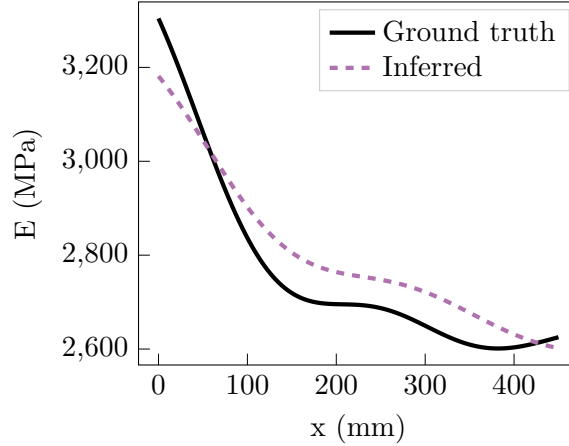
Figure 10: This figure shows the result of the dimensionality-reduced and generalized polynomial chaos-accelerated inference of the beam's Young's modulus E_x. The beam's first eigenvector at the upper surface area serves as the model response and observation data. The solid line shows the ground truth Young's modulus field M^{true} and the dashed line corresponds to the estimated Young's modulus field $\tilde{M}_K$ attained via the maximum a posteriori estimate. Here, the covariance function used to generate the ground truth is employed for training the surrogate and as prior information on the *a priori* unknown spatially varying Young's modulus. The identified field agrees excellently with the ground truth field.

varying stiffness identification results obtained from the academic example are shown together with metrics on the computational effort of our methodology.

The three configurations undergo static analysis with the finite element method to assess the effect of the functional grading in comparison with the homogeneous material. Here, a three-dimensional volume model of a beam with the same geometry as used in Section 3.1 is created using the commercial finite element method code COMSOL. The discretization using quadratic tetrahedral serendipity elements yields 6,327 degrees of freedom. The boundary conditions and loads are applied uniformly across the width of the beam. The yield and von Mises stresses are computed and the safety-margin is obtained as $s = \sigma_y / \sigma_{\text{Mises}}$ along the beam coordinate. Table 4 reports the percentage increases in terms of the minimum safeties $s_{\min}$ of the functionally graded material relative to the homogeneous material for all configurations. These results show that the functional grading improves the safety in the critical regions. The functionally graded safety of configuration 1 exceeds that of the homogeneous part at the clamping, where both material configurations exhibit $s_{\min}$. For configuration 2, the minimum safety lies at the clamping as well, while the minimum safety for configuration 3 is located at the center of the beam. Using the

19

functionally graded material results in a uniform increase in $s_{\min}$ with respect to the homogeneous material throughout the configurations.

	configuration 1	configuration 2	configuration 3
Relative increase of $s_{\min}$	16.7%	16.7%	16.3%

Table 4: The table compares the homogeneous parts with the functionally graded parts with respect to their minimum safeties for each configuration. The minimum safeties corresponding to the functionally graded parts are higher than those of their homogeneous counterparts throughout the configurations. The increase of the minimum safety is calculated as the relative percentage deviation with the homogeneous configuration as reference.

Now, the stiffness is assumed as unknown. All configurations consequently undergo non-destructive testing where the aim is to identify the stiffness. For configuration 2, the baseline procedure described in Section 3.1 is applied. The mean value of the stiffness is assumed as 3×10^3 MPa. The Young's modulus is modeled as homogeneous in y and z direction and only varies along the x-coordinate. The length-scale for the Karhunen-Loève expansion of the inference is chosen as L_2 in accordance with Table 3. Here, the Karhunen-Loève truncation order is set to 5. The finite element model is evaluated for random field realizations connected to the length-scale of configuration 2 $L_2 = 450$ mm. The generalized polynomial chaos surrogate is trained using these finite element model evaluations. Presenting one of the main contributions of this study, the stiffness identifications for configuration 1 and configuration 3 use a transformed version of the surrogate connected to configuration 2. No additional finite element model evaluations are necessary. Merely the Karhunen-Loève expansion must be recomputed with the appropriate length-scale from Table 3 in order to obtain the projection coefficients from Eq. (10) for the surrogate transformation described in Section 2.4. The transformed surrogates following the scheme shown in Figure 11 can now be used for the inference. Table 5 lists the amount of high-fidelity finite element forward model evaluations that are necessary for each inference. Note that only surrogate model evaluations are necessary for the inference involving configuration 1 and configuration 3 with our proposed procedure.

Figure 12 shows the agreement of the identified Young's moduli with the *a priori* unknown ground truth stiffness. The unknown ground truth stiffness is plotted using a solid line and the estimated stiffness uses a dashed style. For configuration 1, the estimation based on the recycled surrogate correctly identifies the trend and character of the ground truth stiffness. However, there
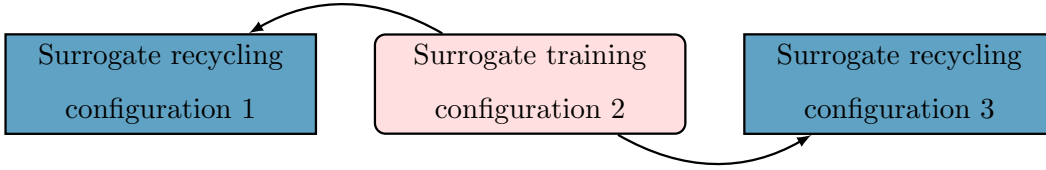
Figure 11: The generalized polynomial chaos surrogate is trained using finite element model evaluations based on the stiffness covariance belonging to the functionally graded part designed for configuration 2. With the known length-scales L_1 and L_3, but without new finite element model evaluations using stiffness samples based on these length-scales, the surrogate trained on configuration 2 can be reused for both configuration 1 and configuration 3.

| Forward model evaluations	configuration 1	configuration 2	configuration 3
Proposed methodology	0	42	0
Conventional surrogate modeling	42	42	42

Table 5: Amount of necessary forward model evaluations comparing the proposed framework to conventional surrogate modeling. The surrogate connects $\boldsymbol{\eta}$ to the beam's first mode shape. Traditionally, the surrogate must be recomputed when the length-scale L changes and consequently, new finite element model evaluations are necessary. With the proposed workflow, no new finite element model evaluations are necessary and one set of evaluations suffices.

is an offset throughout the beam domain of order of magnitude 1×10^2 MPa. The estimation using the surrogate trained on L_2 correctly identifies the trend and character of the ground truth stiffness belonging to configuration 2. However, the inversion underestimates the beam stiffness near the clamping and overestimates it at $x > 100$ mm. Finally, the estimation for configuration 3 based on the recycled surrogate correctly identifies the trend and character of the ground truth stiffness. The maximum stiffness at the center and the minimum stiffness values at the bounds are overestimated by the order of magnitude 1×10^1 MPa. Overall, the lowest error is achieved here.

Overall, the estimations agree well with the reference values. The shapes are excellently approximated for all configurations, while the maximum errors at the respective x-coordinates lie in the range of $1 \times 10^1 - 1 \times 10^2$ MPa. The smallest error over the beam domain is achieved for configuration 3 and the largest error over the domain is attributed to configuration 1. The error for configuration 2 lies in between the error connected to configuration 1 and configuration 3. This is an unexpected result, as no surrogate recycling occurs here. Indeed, the error is proportional to the magnitude of the first two ground truth Karhunen-Loève coefficients and thus depends on the application.
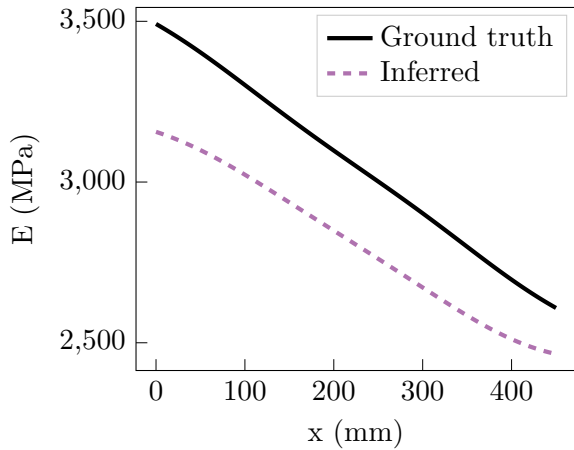
(a) Configuration 1: result of the inference procedure using a recycled surrogate model compared to the *a priori* unknown ground truth stiffness.
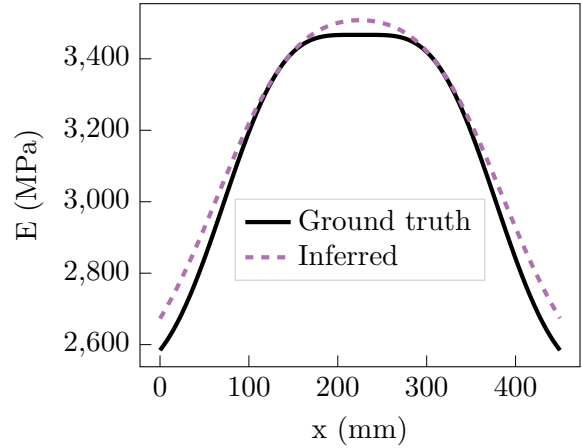
(b) Configuration 3: result of the inference procedure using a recycled surrogate model (dashed) compared to the *a priori* unknown ground truth stiffness (solid).

Figure 12: Bayesian inference results for the non-reference configurations: The *a priori* unknown ground truth stiffness (solid) and the estimated stiffness (dashed) are compared with each other.

5. Discussion and Conclusions

5.1. Discussion

Scrutinizing the results reveals that the proposed stiffness identification procedure succeeded in identifying the stiffness in a mean sense for configuration 2 and configuration 3 with reasonable accuracy, but failed to identify the stiffness correctly in the mean sense for configuration 1. One way of identifying an erroneous offset in the identification results is to carry out a brief cross-check between the mean of the identified stiffness and an experimentally determined eigenfrequency.

The proposed methodology cannot be applied when the geometry or the boundary conditions of the tested structure change. Other methods must be developed to cover these application areas.

Further, there exist scenarios, where employing the proposed method is not necessary. The advantages thrive when forward model evaluations are computationally expensive. This is especially the case for complex geometries and the necessity of fine discretization. If a computationally affordable and sufficiently accurate model exists, the construction of surrogates may not be necessary.

Our academic example uses only three different length-scales. However, the proposed methodology provides more value when many process parameter length-scales are deployed during manufac-

22

turing. The computational cost for constructing the reference surrogate can be viewed as fixed cost
in this context. Further, the fixed cost may be increasingly offset by inference procedures where the
reference surrogate is recycled. Within this analogy, the computational overhead, mainly consisting of Karhunen-Loève expansion computations and likelihood evaluations, corresponds to variable
cost.

5.2. Conclusions

This study used an accelerated method for non-destructively identifying the multi-dimensional
spatially varying stiffness while considering its uncertainty. Here, the structure's mode shapes
served as data. We conclude that

- the method delivers excellent results over the entire structure's domain.

- the method exhibits a significant computational time speedup when compared with procedures evaluating the finite element model at each inference step.

Furthering the state of the art, we formulated a novel methodology for recycling the surrogate
model for the use in theoretically unlimited follow-up inference procedures. This methodology
was based on the estimation of the random field length-scale of filament volume fractions and an
assumption of the equivalence to the material property length-scales. We conclude that

- the methodology delivers excellent results when recycling a surrogate model.

- the methodology scales well for an increasing number of process parameter length-scales and
thus delivers significant further computational cost saving potential for large-scale applications.

Future research should produce a database with process-structure-property relations, where
correlations between the parameters may be extracted such that our method can be employed
with more confidence and the cumbersome integrated computational materials engineering may be
avoided.

23

Statements and Declarations

- This study was financially supported by the German Federal Ministry of Food and Agriculture through the Fachagentur Nachwachsende Rohstoffe e.V. (FNR) (grant number 22009817).

- The authors have no relevant financial or non-financial interests to disclose.

- The raw data generated during the current study are available from the corresponding author upon reasonable request.

CRediT Author Statement

Karl-Alexander Hoppe: Conceptualization, Methodology, Software, Validation, Formal analysis, Investigation, Resources, Writing - Original Draft, Writing - Review & Editing, Visualization, Supervision, Project administration. **Kevin Josef Li:** Methodology, Software, Formal analysis, Investigation, Data Curation, Visualization. **Bettina Chocholaty:** Resources, Writing - Review & Editing. **Johannes D. Schmid:** Resources, Writing - Review & Editing. **Simon Schmid:** Conceptualization, Writing - Review & Editing. **Kian Sepahvand:** Validation. **Steffen Marburg:** Writing - Review & Editing, Supervision, Funding acquisition.

References

[1] H. N. Gupta, R. C. Gupta, A. Mittal, Manufacturing processes, New age international (P) ltd., New Delhi, 2009.

[2] D. Garcia, M. E. Jones, Y. Zhu, Z. Y. Hang, Mesoscale design of heterogeneous material systems in multi-material additive manufacturing, Journal of Materials Research 33 (1) (2018) 58–67. `doi:10.1557/jmr.2017.328`.

[3] Y. M. Marzouk, H. N. Najm, Dimensionality reduction and polynomial chaos acceleration of bayesian inference in inverse problems, Journal of Computational Physics 228 (6) (2009) 1862–1902. `doi:10.1016/j.jcp.2008.11.024`.

[4] F. Uribe, I. Papaioannou, W. Betz, D. Straub, Bayesian inference of random fields represented with the karhunen–loève expansion, Computer Methods in Applied Mechanics and Engineering 358 (2020) 112632. `doi:10.1016/j.cma.2019.112632`.

[5] N. Sundararajan, T. Prakash, M. Ganapathi, Nonlinear free flexural vibrations of functionally graded rectangular and skew plates under thermal environments, Finite Elements in Analysis and Design 42 (2) (2005) 152–168. `doi:10.1016/j.finel.2005.06.001`.

[6] K.-A. Hoppe, M. G. T. Kronthaler, K. Sepahvand, S. Marburg, Identification of a cantilever beam's spatially uncertain stiffness, Scientific Reports 13 (2023) 1169:1–1169:13. `doi:10.1038/s41598-023-27755-5`.
URL `https://doi.org/10.1038/s41598-023-27755-5`

[7] L. Mehrez, A. Doostan, D. Moens, D. Vandepitte, Stochastic identification of composite material properties from limited experimental databases, part ii: Uncertainty modelling, Mechanical Systems and Signal Processing 27 (2012) 484–498. `doi:10.1016/j.ymssp.2011.09.001`.
URL `https://www.sciencedirect.com/science/article/pii/S0888327011003694`

[8] S. Debruyne, D. Vandepitte, D. Moens, Identification of design parameter variability of honeycomb sandwich beams from a study of limited available experimental dynamic structural response data, Computers & Structures 146 (2015) 197–213. `doi:10.1016/j.compstruc.2013.09.004`.
URL `http://doi.org/10.1016/j.compstruc.2013.09.004`

[9] A. Batou, C. Soize, Stochastic modeling and identification of an uncertain computational dynamical model with random fields properties and model uncertainties, Archive of Applied Mechanics 83 (6) (2013) 831–848. `doi:10.1007/s00419-012-0720-7`.
URL `http://doi.org/10.1007/s00419-012-0720-7`

[10] I. Sraj, O. P. Le Maître, O. M. Knio, I. Hoteit, Coordinate transformation and polynomial chaos for the bayesian inference of a gaussian process with parametrized prior covariance function, Computer Methods in Applied Mechanics and Engineering 298 (2016) 205–228. `doi:10.1016/j.cma.2015.10.002`.

[11] A. Siripatana, O. Le Maitre, O. Knio, C. Dawson, I. Hoteit, Bayesian inference of spatially varying manning's n coefficients in an idealized coastal ocean model using a generalized karhunen-loève expansion and polynomial chaos, Ocean Dynamics 70 (8) (2020) 1103–1127. `doi:10.1007/s10236-020-01382-4`.

[12] S. M. Hashemi, S. Parvizi, H. Baghbanijavid, A. T. Tan, M. Nematollahi, A. Ramazani, N. X. Fang, M. Elahinia, Computational modelling of process–structure–property–performance relationships in metal additive manufacturing: A review, International Materials Reviews 67 (1) (2022) 1–46. `doi:10.1080/09506608.2020.1868889`.

[13] T. Gatsos, K. A. Elsayed, Y. Zhai, D. A. Lados, Review on computational modeling of process–microstructure–property relationships in metal additive manufacturing, Jom 72 (1) (2020) 403–419. `doi:10.1007/s11837-019-03913-x`.

[14] W. Gao, Y. Zhang, D. Ramanujan, K. Ramani, Y. Chen, C. B. Williams, C. C. Wang, Y. C. Shin, S. Zhang, P. D. Zavattieri, The status, challenges, and future of additive manufacturing in engineering, Computer-Aided Design 69 (2015) 65–89. `doi:10.1016/j.cad.2015.04.001`.

[15] E. Louvis, P. Fox, C. J. Sutcliffe, Selective laser melting of aluminium components, Journal of Materials Processing Technology 211 (2) (2011) 275–284. `doi:10.1016/j.jmatprotec.2010.09.019`.

[16] C. Ward, Materials genome initiative for global competitiveness, in: 23rd Advanced Aerospace Materials and Processes (AeroMat) Conference and Exposition, Vol. 202, ASM International, OH, 2012.

[17] P. Fratzl, R. Weinkamer, Nature's hierarchical materials, Progress in Materials Science 52 (8) (2007) 1263–1334. `doi:10.1016/j.pmatsci.2007.06.001`.

[18] G. Gronau, S. T. Krishnaji, M. E. Kinahan, T. Giesa, J. Y. Wong, D. L. Kaplan, M. J. Buehler, A review of combined experimental and computational procedures for assessing biopolymer structure–process–property

relationships, Biomaterials 33 (33) (2012) 8240–8255. `doi:10.1016/j.biomaterials.2012.06.054`.

[19] J. Song, J. Shanghvi, P. Michaleris, Sensitivity analysis and optimization of thermo-elasto-plastic processes with applications to welding side heater design, Computer methods in applied mechanics and engineering 193 (42-44) (2004) 4541–4566. `doi:10.1016/j.cma.2004.03.007`.

[20] S. W. Cranford, M. J. Buehler, Shaky foundations of hierarchical biological materials, Nano Today 6 (4) (2011) 332–338. `doi:10.1016/j.nantod.2011.07.001`.

[21] B. Patham, P. H. Foss, Thermoplastic vibration welding: Review of process phenomenology and processing–structure–property interrelationships, Polymer Engineering & Science 51 (1) (2011) 1–22. `doi:10.1002/pen.21784`.

[22] W. Yan, S. Lin, O. L. Kafka, Y. Lian, C. Yu, Z. Liu, J. Yan, S. Wolff, H. Wu, E. Ndip-Agbor, et al., Data-driven multi-scale multi-physics models to derive process–structure–property relationships for additive manufacturing, Computational Mechanics 61 (5) (2018) 521–541. `doi:10.1007/s00466-018-1539-z`.

[23] T. Moges, G. Ameta, P. Witherell, A review of model inaccuracy and parameter uncertainty in laser powder bed fusion models and simulations, Journal of manufacturing science and engineering 141 (4). `doi:10.1115/1.4042789`.

[24] M. M. Francois, A. Sun, W. E. King, N. J. Henson, D. Tourret, C. A. Bronkhorst, N. N. Carlson, C. K. Newman, T. Haut, J. Bakosi, et al., Modeling of additive manufacturing processes for metals: Challenges and opportunities, Current Opinion in Solid State and Materials Science 21 (4) (2017) 198–206. `doi:10.1016/J.COSSMS.2016.12.001`.

[25] M. F. Horstemeyer, S. Sahay, Integrated Computational Materials Engineering (ICME) for Metals, John Wiley & Sons, Ltd, Hoboken, 2018. `doi:10.1002/9781119018377`.

[26] S. Ghosh, Predictive modeling of solidification during laser additive manufacturing of nickel superalloys: recent developments, future directions, Materials Research Express 5 (1) (2018) 012001. `doi:10.1088/2053-1591/aaa04c`.

[27] S.-H. Ahn, M. Montero, D. Odell, S. Roundy, P. K. Wright, Anisotropic material properties of fused deposition modeling abs, Rapid prototyping journal 8 (4) (2002) 248–257. `doi:10.1108/13552540210441166`.

[28] R. Setter, F. Riedel, W. Peukert, J. Schmidt, K. Wudy, Infiltration behavior of liquid thermosets in thermoplastic powders for additive manufacturing of polymer composite parts in a combined powder bed fusion process, Polymer Composites 42 (10) (2021) 5265–5279. `doi:10.1002/pc.26221`.

[29] M. Rafiee, R. D. Farahani, D. Therriault, Multi-material 3d and 4d printing: a survey, Advanced Science 7 (12) (2020) 1902307. `doi:10.1002/advs.201902307`.

[30] T. J. Sullivan, Introduction to uncertainty quantification, Vol. 63, Springer International Publishing, Cham, 2015. `doi:10.1007/978-3-319-23395-6`.

[31] M. Alnæs, J. Blechta, J. Hake, A. Johansson, B. Kehlet, A. Logg, C. Richardson, J. Ring, M. E. Rognes, G. N. Wells, The fenics project version 1.5, Archive of Numerical Software 3 (100). `doi:10.11588/ans.2015.100.20553`.

[32] C. E. Rasmussen, C. K. I. Williams, Gaussian Processes for Machine Learning, The MIT Press, Cambridge, MA, 2005. `doi:10.7551/mitpress/3206.001.0001`.

[33] M. Abramowitz, I. A. Stegun, Handbook of Mathematical Functions with Formulas, Graphs, and Mathematical Tables, Dover Publications Inc., New York, 1965.